Advanced reconstruction of attenuation maps using SPECT emission data only

André Salomon[a,b], Andreas Goedicke[a], Til Aach[b]
[a]Philips Research Laboratories, Molecular Imaging Systems, Weisshausstrasse 2, Aachen, Germany;
[b]Institute of Imaging & Computer Vision, RWTH Aachen University, Aachen, Germany

ABSTRACT

Today, attenuation corrected SPECT, typically performed using CT or Gadolinium line source based transmission scans, is more and more becoming standard in many medical applications. Moreover, the information about the material density distribution provided by these scans is key for other artifact compensation approaches in advanced SPECT reconstruction. Major drawbacks of these approaches are the additional patient radiation and hardware/maintenance costs as well as the additional workflow effort, e.g. if the CT scans are not performed on a hybrid scanner. It has been investigated in the past, whether it is possible to recover this structural information solely from the SPECT scan data. However, the investigated methods often result in noticeable image artifacts due to cross-dependences between attenuation and activity distribution estimation. With the simultaneous reconstruction method presented in this paper, we aim to effectively prevent these typical cross-talk artifacts using a-priori known atlas information of a human body.

At first, an initial 3D shape model is coarsely registered to the SPECT data using anatomical landmarks and each organ structure within the model is identified with its typical attenuation coefficient. During the iterative reconstruction based on a modified ML-EM scheme, the algorithm simultaneously adapts both, the local activity estimation and the 3D shape model in order to improve the overall consistency between measured and estimated sinogram data. By explicitly avoiding topology modifications resulting in a non-anatomical state, we ensure that the estimated attenuation map remains realistic.

Several tests with simulated as well as real patient SPECT data were performed to test the proposed algorithm, which demonstrated reliable convergence behaviour in both cases. Comparing the achieved results with available reference data, an overall good agreement for both cold as well as hot activity regions could be observed (mean deviation: -5.98%).

Keywords: cardiac SPECT, attenuation correction, consistency conditions, myocardial perfusion imaging

1. INTRODUCTION

Attenuation correction in SPECT is becoming more and more widely accepted by clinicians in order to reduce first order reconstruction artifacts. In combination with resolution recovery and scatter correction techniques, some encouraging progress concerning quantitative SPECT imaging was made [1]. One major drawback one has to take into account is the need of accurate information about the attenuation in the patient to provide attenuation- and scatter correction [2]. Especially in cardiac/thorax SPECT imaging, the tissue distribution is fairly non-uniform and so inaccuracies in the attenuation map or its total absence during reconstruction might lead to severe artifacts impacting the diagnostic value of the method [3][4]. Today, attenuation information is typically acquired using additional scanner equipment like CT or additional hardware, like Gadolinium point or line sources. Thereby, even if it is much cheaper, the second option has also its drawbacks, namely its limited accuracy and the burden of periodical service costs for exchange and maintenance of the Gadolinium source. An increasing challenge for the market of myocardium perfusion imaging in SPECT is the decreasing cost-difference to the (still) more expensive PET modality. Because PET often provides better image quality for similar applications, the number of false diagnoses is often reduced compared to SPECT. This leads to a significant reduction of expensive follow-up diagnostics, like invasive coronary arteriography, and thus to evident cost savings [5]. In consequence, SPECT manufacturers always try to find cost-effective solutions to improve the performance of their

scanners, in order to remain or even increase the diagnostic value of this mature modality and to keep or extend their market share.

Alternatives for determination of μ-maps directly from the SPECT projection data, e.g. of the thorax region, have been investigated [6]. These methods are based on so called consistency conditions, which are mathematical formulations of the fact that the attenuation information is (partially) already contained in the SPECT emission data and thus can be extracted to some extent with additional computational effort. This is due to the fact that, from an ideal, mathematical point of view (i.e. neglecting Poisson- and quantization-noise), each practically relevant, non-symmetric combination of activity and attenuation-distribution leads to a unique SPECT sinogram. Further details can be found in [7]. It has also been shown, that this holds not only for 360-degree-acquisitions, but also limited scan angles down to 180 degrees [8].

Early approaches to extract attenuation information out of emission data try to minimize a penalty function by fitting only a few parameters of a simplified structure model consisting of ellipses [9][10]. These methods are based on a rather complex relationship between the estimated attenuation, the activity map and the measured projections. However, according to its complexity, the usability of this consistency condition seems to be limited for practical applications. The attenuation maps generated with this approach provide a homogeneous attenuation behavior and thus show some noticeable deviations from reality. An alternative method was proposed by Kudo et al. [11]. Here, a different penalty function, also based on the consistency between the measured and the estimated sinogram, is iteratively minimized by random changes to the attenuation map. Since the method makes use of some restrictions to the topology of the estimated attenuation map, it allows for the reduction of most inherent cross-talk effects between the estimated activity and attenuation. Unfortunately, the computational effort for this interesting technique is very high and it shows a slow convergence behavior. This is mainly because of the chosen optimization scheme - Simulated Annealing (SA) - which causes a random trial-and-error like modification of the topology. In addition, it is non-trivial to find optimal convergence parameters for the SA algorithm. Finally, in 3D- instead of 2D-reconstruction, the degree of freedom for each labeled region increases remarkably. Thus the computational effort required for the consistency validation is also increased by factors up to the number of transaxial slices.

Recent methods aim to simultaneously reconstruct correction factors for both estimated activity and attenuation. Since the problem in practice is highly underdetermined (or “ill-posed”), some approaches use e.g. the Tikhonov Regularization in order to generate an adequately realistic estimation of the attenuation [12]. Others provide methods to consider noise properties during the reconstruction in form of modified gradient ascent- and EM-algorithms [13][14].

The major limitations of all these methods are the inherent cross-dependences between the activity and attenuation distributions. These inherent cross-talk effects lead to artifacts in the attenuation map [14]. The simultaneous reconstruction method proposed in this paper aims to reduce these artificially introduced artifacts.

2. METHODOLOGY

The whole concept of the proposed method is motivated by previously discussed advantages and disadvantages of already published methods.

The labelling concept of Kudo et al. [11], together with its strict organ topology preservation, is extended to a fully 3D active contour model, which is set up and registered with an initial SPECT reconstruction data set in the first step. Each organ region is labelled with a typical attenuation value, depending on its tissue type (lung, bone, soft tissue, air). The active contour model is derived from a software body model representing a standard male or female patient. In this way, an anatomically reasonable start configuration is generated.

The second step iteratively improves the estimated region boundary of each organ as well as the outer body shape and simultaneously uses the currently estimated contour for scatter- and attenuation-corrected activity reconstruction. The method makes use of a modified ML-EM algorithm as described in [16] to perform several iterations of activity map reconstruction. Furthermore, the gradient-ascent approach of [13] is used to compute a correction field for the present attenuation map. This correction field finally provides information about which parts of the estimated contours have to grow or shrink in order to further improve the match between (forward-) projected activity and measured SPECT projections. In the following these steps are described in more detail.

2.1 Setup of initial 3D-contour

Since most SPECT reconstructions without attenuation correction - especially cardiac SPECT scans - provide a robust location of organ (sub-) structures like the left heart ventricle, the liver or the kidneys, it is in principle possible to create a good initial guess for the attenuation map. This map can be segmented into a small number of different regions, whose attenuation behaviour is assumed to be homogeneous. The initial organ contours (lungs, bones, soft-tissue, etc.) and the outer boundary of the patient are estimated using the following steps, including reconstruction (without attenuation correction) and usage of a-priori information:

I. Estimation of the outer body boundaries

II. Search position and orientation of heart and liver

III. Fitting atlas-based information of an average patient to the measured data

Estimation of the outer patient boundary is done by a combination of binary segmentation and reconstruction. First, using a threshold value *t,* computed as the first local minimum of the histogram of the measured sinogram data, it is decided whether a voxel is localized inside the patient or not [15]. Then, the binary segmentation of the sinogram is determined as:

$$\hat{p}_j = \begin{cases} 1, & if\ p_j \geq t \\ 0 & else \end{cases} \quad | \forall j \in J \tag{1}$$

where p_j indicates one pixel of the measured sinogram. The resulting binary sinogram is reconstructed using one iteration of the OS-EM algorithm [17] which simplifies to:

$$\lambda_i = \begin{cases} 1, & if \prod_{p \in P} \sum_{j \in J_p} \hat{p}_j f_{ij} > 0 \\ 0, & else \end{cases} \quad | \forall i \in I \tag{2}$$

Here, f_{ij} denotes the sensitivity of detector pixel j towards image voxel i and J_p is referred to as set of all detector pixels labelled with projection angle with index p. In our implementation, we have chosen the number of OS-EM subsets equal to the number of projection angles.

This simple reconstruction of the outer boundaries delivers reasonable results only for convex contour parts. Concave parts of the contour are later corrected during the iterative optimization process. Other methods which attempt to reconstruct also concave boundaries like in [15] are expected to fail in cases where e.g. the gap between the female breasts has to be detected correctly.

Position and orientation of heart and liver can be computed by a template matching algorithm between a-priori models and an estimate of the activity distribution. The previously derived slice-wise convex body contour hull is used in this step as start estimate of the attenuation map μ_i, only containing the attenuation value for water (0.15 cm^{-1} @ 140.5keV) and air (set to zero). To get a first guess of the activity distribution, two iterations of the attenuation corrected OS-EM algorithm are computed, which can be expressed as:

$$\lambda_i^{(n+1)} = \lambda_i^{(n)} \frac{1}{\sum_{j \in J_b} f_{ij}^{\mu}} \sum_{j \in J_b} \frac{p_j f_{ij}^{\mu}}{\sum_{\hat{i} \in I} f_{\hat{i}j}^{\mu} \lambda_{\hat{i}}^{(n)}} \quad | \forall b \tag{3}$$

Here, b is referred to as index of the subsets, and f_{ij}^{μ} contains the impact of the uniform attenuation μ_i.

This leads to an activity map where the heart as well as the liver can be detected using template matching algorithms, providing information about the position and orientation of both organs.

Fitting of atlas-based data can now be performed using the outer boundary of the patient and the previously computed information about the extension and localization of the heart and the liver. We used the NCAT-phantom [18] – a computer model of a standard adult male/female patient – to provide coarse atlas-information containing mainly relevant organs: lungs, heart, liver and bony structures. According to the given guess for the orientation and position of heart and

liver in the patient data a rigid transformation of the atlas data is performed. In combination with a simple collision detection regarding the outer patient boundary, a good initial fit of the atlas model to the patient data can be found in most cases. Thereby, the estimated extent of the lung tissue can be prevented from overlapping with regions of the relatively high active heart or liver. Otherwise, this overlap and the resulting inaccuracies during attenuation correction would lead to artifacts, such as e.g. a local overestimate of the activity in the myocardium.

Finally**,** the initial body and organ contours are transformed to a 3D grid structure consisting of a number of connected mesh-points. In the following, these mesh-points are referred to as *vertices,* and at least three of them determine a so called *face*, respectively. Each organ contains a typical, a-priori attenuation value according to its tissue-type and the isotope-specific emission energy. Vice-versa, a 3D voxel-based attenuation map can be generated from the model at arbitrary image resolution and be used for attenuation correction during reconstruction processes.

2.2 Reconstruction of activity and attenuation

The second part of the proposed method iteratively reconstructs the activity and simultaneously performs modifications to the estimated attenuation map according to the following steps:

I. Reconstruct the activity distribution given the present attenuation map model
II. Check consistency between measured and estimated emission data
III. Calculate correction factors for each attenuating voxel
IV. Modify active contour model according to the correction factors
V. Generate a new attenuation map and go back to step I again

The reconstruction of activity distribution is done by applying several iterations of the ML-EM algorithm [16][1], which can be formulated as:

$$\lambda_i^{(n+1)} = \lambda_i^{(n)} \frac{1}{\sum_{j\in J} f_{ij}^{\mu^{(n)}}} \sum_{j\in J} \frac{p_j f_{ij}^{\mu^{(n)}}}{\sum_{\hat{i}\in I} f_{\hat{i}j}^{\mu^{(n)}} \lambda_{\hat{i}}^{(n)}} \tag{4}$$

Here, the impact of the attenuation is considered in the entries of the system-matrix $f_{ij}^{\mu^{(n)}}$, where $\mu^{(n)}$ describes the usage of the present attenuation map estimate. The main reason for using ML-EM and not OS-EM in principle is the poor convergence behaviour of the latter in cases in which the system-matrix does not match with reality. At least at the beginning of the procedure, where only a coarse estimate of the true attenuation map exists, OS-EM tends to result in an inaccurate weighting of the attenuation information contained in the emission data. As a result, we found that no suitable correction factors can be further extracted and poor convergence is obtained if OS-EM is used in this step in practice.

The consistency check between the overall estimation of both distributions and the measured data is performed by calculating the squared difference of the sinograms on a pixel-by-pixel basis. The overall sum as proposed in formula (7) in [11] can be also expressed as:

$$E = \sum_{j\in J} \left\| \tilde{p}_j - p_j \right\|^2 \to 0 \tag{5}$$

$$\tilde{p}_j = \sum_{i\in I} f_{ij}^{\mu^{(n)}} \lambda_i^{(n)} \tag{6}$$

where $\tilde{p}_j$ denotes the attenuated forward projection of the activity distribution. The algorithm has to ensure that E is decreasing during reconstruction, in order to improve the overall consistency between measured and estimated data. It is not necessary in general to calculate the consistency, but it may be used e.g. as a stopping-criterion for the whole algorithm.

The calculation of correction factors K_i^{μ} for the attenuation map in the patient is again done using an ML-EM approach with a special weighting scheme as proposed in [13]. The discrete projector-backprojector can be also formulated as:

$$K_i^{\mu} = \frac{1}{\sum_{j \in J} b_{ij}} \sum_{j \in J} \left[\left(1 - \frac{p_j}{\sum_{\hat{i} \in I} f_{\hat{i}j}^{\ \mu^{(n)}} \lambda_{\hat{i}}^{(n)}} \right) \cdot b_{ij} \right], \tag{7}$$

$$b_{ij} = \sum_{\hat{i} \in I_{ij}^*} f_{\hat{i}j}^{\ \mu^{(n)}} \lambda_{\hat{i}}^{(n)} \quad , \quad I_{ij}^* = \left\{ I \,\middle|\, u_i^j > u_{\hat{i}}^j ; \hat{i} \in I \right\}$$

where u_i^j represents the smallest distance between image voxel *i* and detector pixel *j* and I^*_{ij} indicates the discrete integration along the opposing direction to the detector. The weighting factors b_{ij} are interpreted as the sensitivity of attenuation coefficient μ_i regarding a change in the sinogram at pixel *j*.

The modifications to the active contour, resulting in an update of the attenuation map, are performed for each mesh-point separately. In contrast to the proposed method in [13], resulting modifications do not affect all voxels of the attenuation volume, but only those which are close to an organ boundary. This is realized by applying modifications to the boundary mesh structure only. Subsequently, the mesh structure is transferred again into an (updated) attenuation map, with maybe slightly changed organ boundaries. In order to determine the new position of each *vertex*, we propose to integrate along the organ-boundaries or, respectively, the faces of the mesh:

$$\overline{K}_f = \frac{\sum_i c_{if} K_i}{\sum_i c_{if}}, \tag{8}$$

where $f \in F$ is the index of a face and c_{if} represents the intersection area between voxel *i* and face *f*.

Alternatively, one can also integrate over a suitable extended 3D-region in order to decrease the impact of statistical noise. The sign of $\overline{K}_f$ indicates weather local attenuation should be decreased or increased. For each face *f*, a perpendicular vector $\vec{d}_f$ is calculated, whose length is correlated to the previously computed integration value $\overline{K}_f$.

$$\vec{d}_f = \overline{K}_f \cdot \frac{\vec{r}}{\|\vec{r}\|} \quad \left| \quad (\vec{r} \perp f), \right. \tag{9}$$

where vector $\vec{r}$ points to the less attenuating region from view of face *f*, respectively. Finally, these vectors are locally averaged between all faces each *vertex* belongs to:

$$\vec{\nabla}_v = \frac{\sum_{f \in F_v} \vec{d}_f}{\|F_v\|} \tag{10}$$

The result, $\vec{\nabla}_v$, is the correction vector for a vertex $\vec{v}$ with index *v*. The update step can therefore be expressed as:

$$\vec{v}_v^{(n+1)} = \vec{v}_v^{(n)} + \vec{\nabla}_v \tag{11}$$

Please note that in this step it is also required to perform collision detection between neighbouring surfaces in order to preserve the topological consistency. This can be simply realized by neglecting local mesh updates which would result in a local overlap of different organ boundaries.

The generation of a new attenuation map is realized by a homogeneous filling of all voxels inside an organ region with the corresponding attenuation value. In our case, given the granularity of the model used, each body/organ region is filled with the attenuation coefficient for either air, soft-, bone- or lung-tissue. This completes one iterative optimization step and the algorithm continues the next iteration with the modified estimations as long as any predefined stopping-criterion is fulfilled

3. DATA

3.1 Monte-Carlo simulated data

For a first evaluation of the proposed method, Monte Carlo simulations have been performed to provide the required input data. Again, we used the NCAT software phantom to generate 'patient like' data sets of an average female body. Projection data of this phantom have subsequently been generated using our own SPECT simulation framework which is based on GEANT4 - a software toolkit developed for simulating the passage of particles through material objects. GEANT4 was developed at CERN and initially intended for detector design in high-energy physics. Due to its extension to low energy particle physics it is now also widely used in many nuclear physics related areas like nuclear medicine and bio-physics. This toolkit has been efficiently accelerated using a modified and extended version of Forced Detection, a variance reduction approach which remarkably reduces the overall simulation effort, especially for SPECT [19].

The whole simulation has been split up in 16 equidistant gates covering different phases of the respiratory and heart motion. The frequency of the latter was assumed to be five times higher than the simulated respiratory motion frequency (heart: 1s, breathing: 5s). Coronal and transverse sections of the distribution of activity and attenuation are shown in Figure 1. The Tc99m activity contrast ratios between body-background, lung and heart tissue were set to 10:8:100. Furthermore, the stomach and all digestive organs were assumed to be filled with air.

Two cases, a circular 360-degree-trajectory and a circular 180-degree-trajectory with 128 projections each have been simulated with a detector resolution of 128x128 for each projection. For the detector, a standard NaI-scintillation camera with an LEHR (Low Efficiency High Resolution) hex-collimator has been chosen. The total number of detected particles within the photopeak window (127 keV…153 keV) was $13.92*10^6$ in the case of the 360-degree-trajectory, and $13.74*10^6$ in the case of the 180-degree-trajectory. Note that the detected sinogram has been cropped near the shoulders of the phantom in order to emulate typical truncation effects.

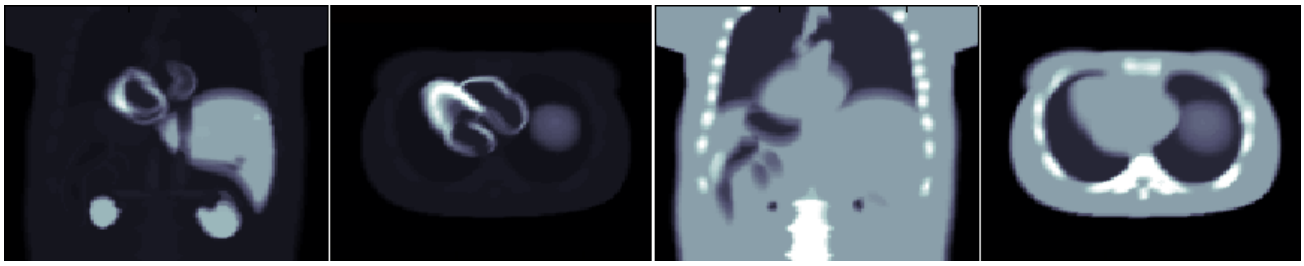

Figure 1: Reference NCAT Phantom data. Simulated activity (left: coronal, transverse view) and attenuation (right: coronal, transverse view) distribution for Tc99m (140.5 keV)

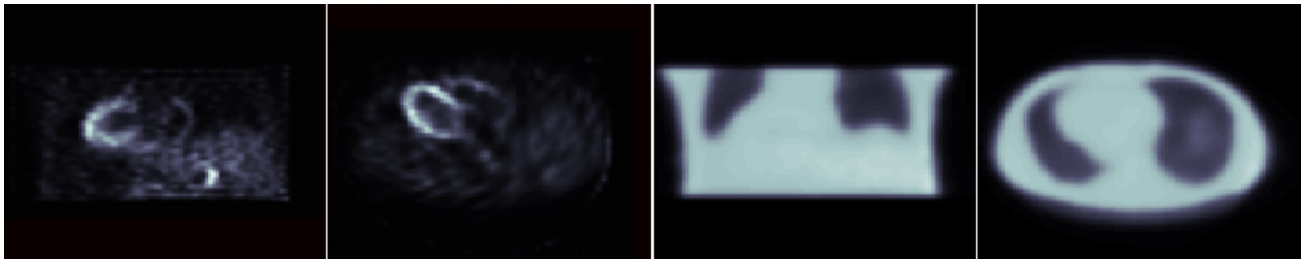

Figure 2: Reconstructed clinical patient 180-degree-data (left) using the attenuation map for Tc99m (140.5 keV) measured with a line source (right).

3.2 Clinical patient data

In addition to the simulated data, real patient data measured with a Philips Cardio MD have been used to evaluate the proposed algorithm for its applicability in clinical practice. Since the real activity distribution in the patient is unknown, the measured SPECT sinogram has been reconstructed using a separate attenuation map (Figure 2). This attenuation map was generated on a Philips Vantage scanner using a Gadolinium line source and is further used as reference data set. The total number of detected counts within the photopeak window of this Tc99m cardiac SPECT scan was $5.94*10^6$. The data acquisition has been performed with a static dual-head SPECT camera and an elliptic trajectory located as close to the heart as possible with a total scanning range of 180 degrees. The data set consisted of 64 projections and the final image resolution for each projection was 64x64 pixels.

4. RESULTS

4.1 Iterative reconstruction of Monte-Carlo simulated data

Several test runs with different initial attenuation distributions have been performed to show the convergence of the proposed optimization algorithm. As an example, Figure 3 below shows the initial attenuation distribution of one of the 360 degree trajectory datasets (see 3.1) with underestimated lung sizes of ~10mm in each direction. Furthermore, for the initial attenuation distribution, only the convex body shape was used as described in 2.1. By iterative optimization of both, activity and attenuation, the overall error as formulated in formula (5) could be decreased by 32.8% (from a total value of $3.9827*10^7$ to $2.6755*10^7$). Figure 4 shows the final reconstructed activities under usage of the initial and the optimized attenuation map. The achieved enhancement is more visible in the differences between the expected and reconstructed activity distributions, before and after the optimization (see Figure 5). The average relative error in the activity towards usage of the reference attenuation map is +25.63% in case of the initial and -5.976% in case of the optimized attenuation. A more detailed view on that is given in Figure 6, showing a line plot profile of a selected cross-sectional slice. The curves represent the reconstructed activities under usage of the different attenuation maps (as shown in Figure 3) as well as without any attenuation correction. The achieved improvement is clearly visible by the good fit between the optimized and the reference curve (black arrows indicate the maximum values).

Figure 3 also displays an additional artifact in the estimated distributions near the shoulders of the patient (see white arrows). These artifacts are caused by truncation of some projections. The algorithm tries to explain the missing (cropped) radiation in these projections by higher attenuation values and generates artifacts in the activity distribution (see white arrows in Figure 4). So, in the example presented, this effect is automatically compensated by an increase (instead of a decrease) of the bone-extents in those truncated transaxial slices. However, since these truncation artifacts only occur in slices at the upper edge of the FOV (in this case), the activity distributions within the interesting regions (e.g. in the myocardium) are almost not affected at all.

In order to demonstrate what happens if the topology of the organ model is inaccurate in terms of initial tissue classification, Figure 5 contains another artifact that has become visible near the lower boundary of the heart after the iterative optimization (see white arrow). The initial estimation did not explicitly contain a stomach model so it was assumed as being filled with soft-tissue like material. In contrast to this, the reference attenuation and thus the Monte-Carlo simulation contained much lower attenuation values in the stomach, due to enclosed air (see black arrow in Figure 3). This inaccuracy in the model results in some remaining overestimations of the optimized activity distribution (see white arrow in Figure 5), which also impacts the reconstructed activity in the myocardium.

The method was further tested for a variety of different initial mismatches concerning the lung extents (both oversized / left lung under- and right lung oversized). All reconstructions showed similar results using 360-degree-acquired SPECT data.

In case of 180-degree-acquired data, the algorithm partially tries to compensate inconsistencies, caused by differences between the initial and the true lung extent, with modifications to the outer boundaries and vice versa. This is due to the fact that 180-degree-sinograms contain less information about the attenuation distribution and thus, in practice, it makes nearly no difference to the sinogram and consistency if e.g. the lungs are extended or the outer boundary is reduced between the detector and the myocardium. Finally, in 180-degree-acquisitions, the initial estimation has to be more accurate than in 360-degree-scans in order to obtain a realistic estimate of the attenuation distribution. Nevertheless, even misalignments between estimated and reference attenuation had only a minor impact on the reconstructed heart activity distribution.

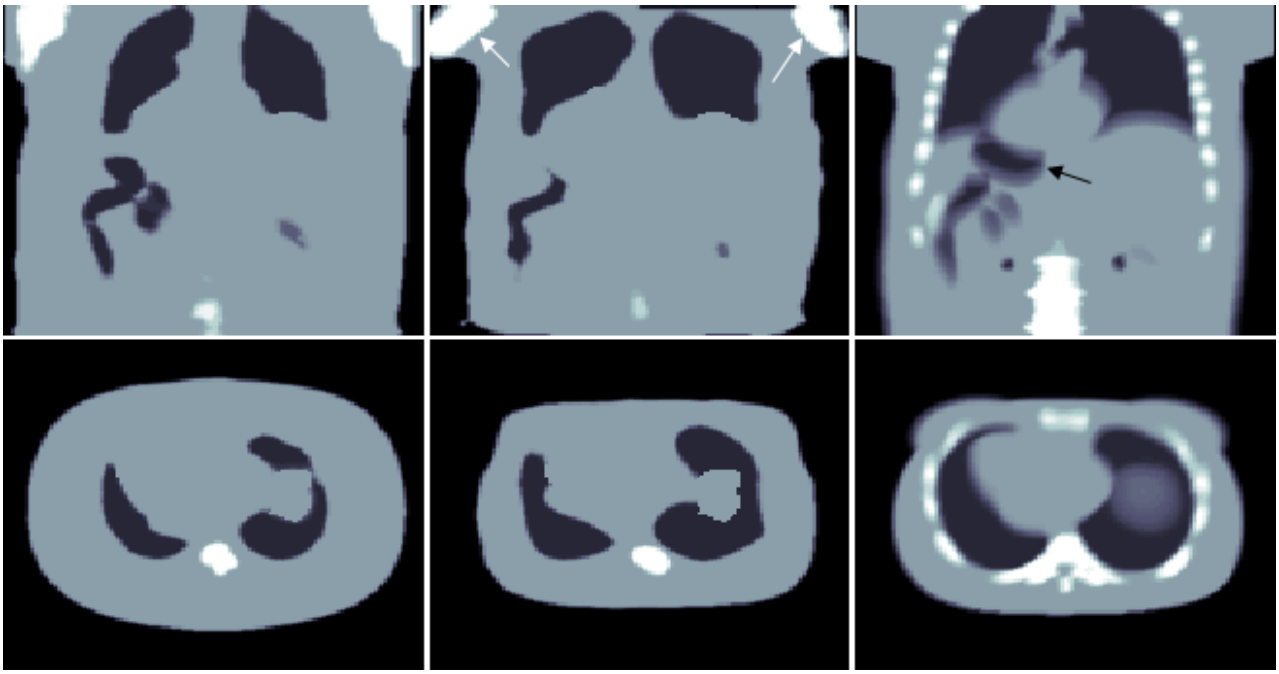

Figure 3: Coronal (top row) and transverse (bottom row) slices of the initial (left), optimized (middle) and reference (right) attenuation map of a simulated 360-degree-acquisition

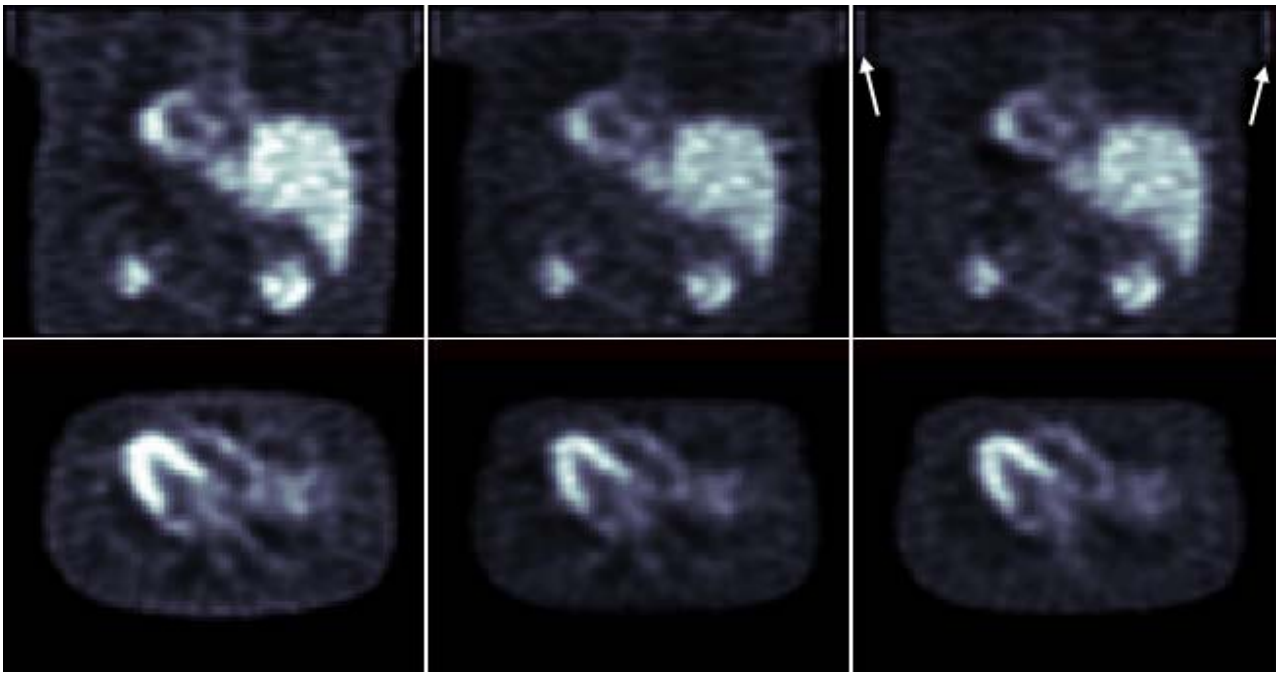

Figure 4: Initial (left: coronal, transverse view), optimized (middle: coronal, transverse view) and reference (right: coronal, transverse view) reconstructed activity of a simulated 360-degree-scan

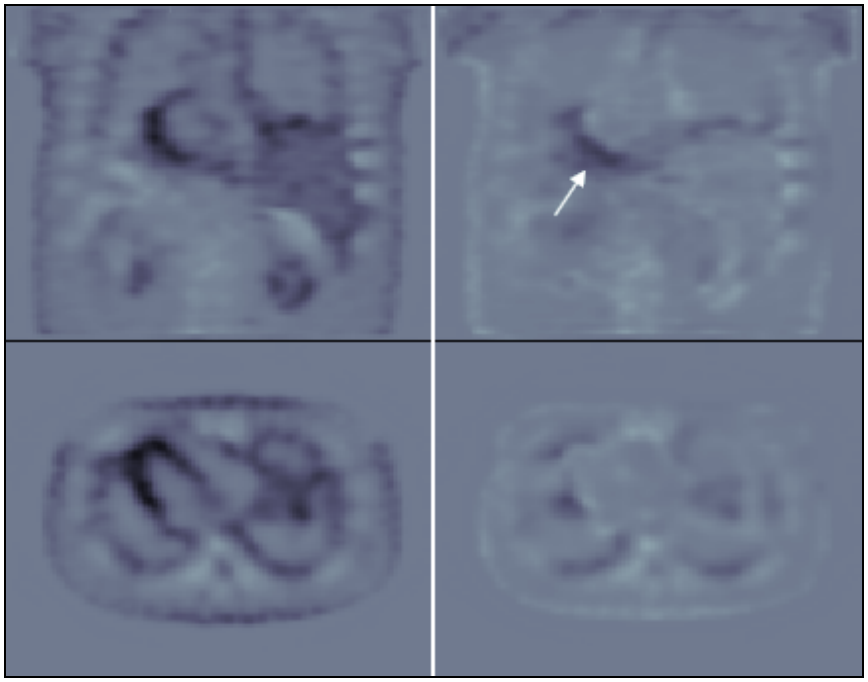

Figure 5: Evaluation of 360-degree-data. On the left side: difference images between the activities reconstructed using the initial attenuation map (Figure 4 left) and using the reference attenuation map. On the right side: differences images between the optimized reconstructed activity (Figure 4 right) and the reconstructed reference activity image. A shift to black indicates too high estimated activity values, a shift to light gray indicates a local lack of activity.

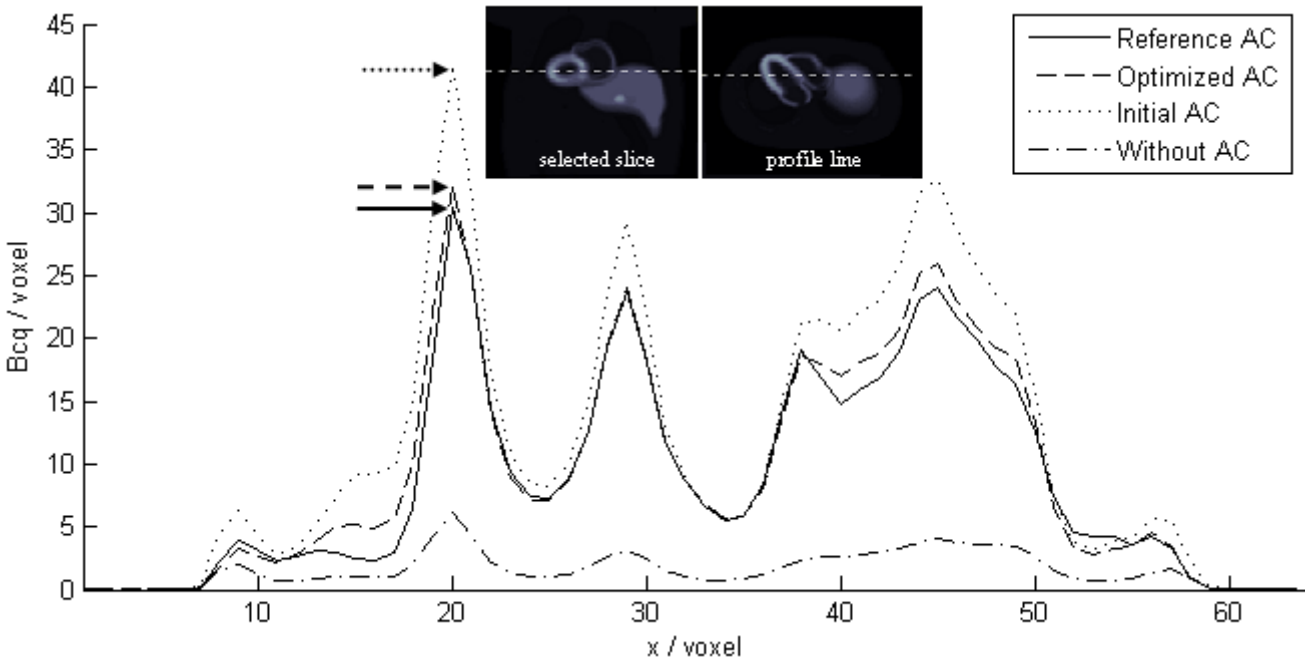

Figure 6: Comparison between the reconstructed activity plot profiles generated using different attenuation maps for attenuation correction (AC). The displayed lines represent the activity at the dotted lines shown in a coronal and transverse cross-section at the upper image of the plot.

4.2 Iterative reconstruction of clinical patient data

After registration of the reference NCAT phantom data and the measured patient data, a slight misestimation of the lung volume can be observed (compare volumes marked with white arrows and reference distribution right in Figure 7). Note that the reference attenuation map itself was not used as an input for the proposed iterative scheme. In this example, the algorithm finally improved the estimation of the reconstructed activity by reducing the lung volumes and adapting the outer boundaries of the body. However, the effect of this optimization towards the cardiac activity distribution has shown to be less significant than for data acquired on a 360-degree-trajectory. So the optimization process sometimes has nearly no effect on the reconstruction accuracy. We also investigated the overall sensitivity of the final activity estimation towards slight changes (misalignments) in the attenuation map. The results confirmed that the impact was noticeably lower for scan data acquired on a 180-degree-trajectory (see Figure 8) compared to data acquired on a 360-degree-trajectory (see Figure 6). The main reason for this is that in practice the attenuation between the detector and the heart is less variant than in 360-degree-scans where the measured radiation, in average, is effected by larger volumes of lung and bone tissue.

In the given patient data set, the activity estimation computed using the optimized attenuation map again shows a clear improvement compared to the one generated with initial attenuation map (see Figure 8, black arrows indicate maximum values). The absolute accumulated activities inside the myocardium showed a mean difference of -6.59% for usage of the initial- and +2.44% for usage of the optimized attenuation map. Again, the improvement was mainly realized by adapting the lung region in the model.

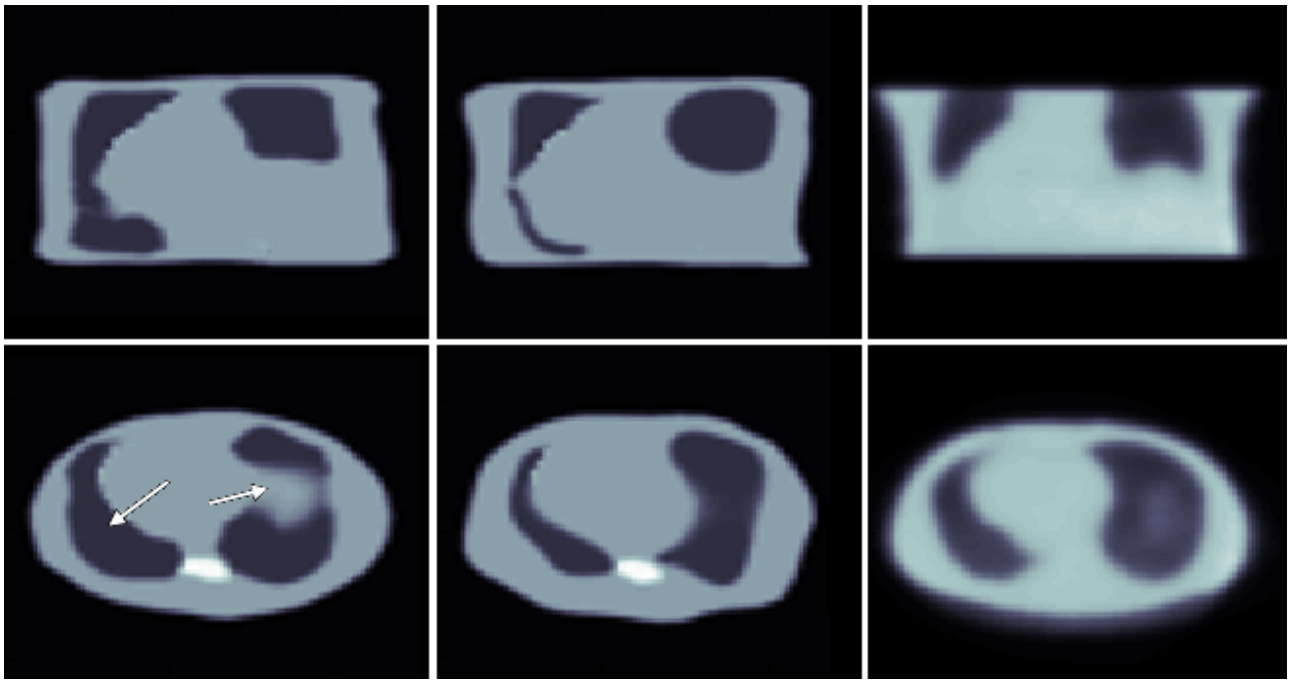

Figure 7: Coronal (upper row) and transverse (lower row) section of the initially estimated attenuation map (left), the iteratively optimized attenuation map (middle) and the reference distribution (post-processed attenuation map generated using a Gadolinium line source, right).

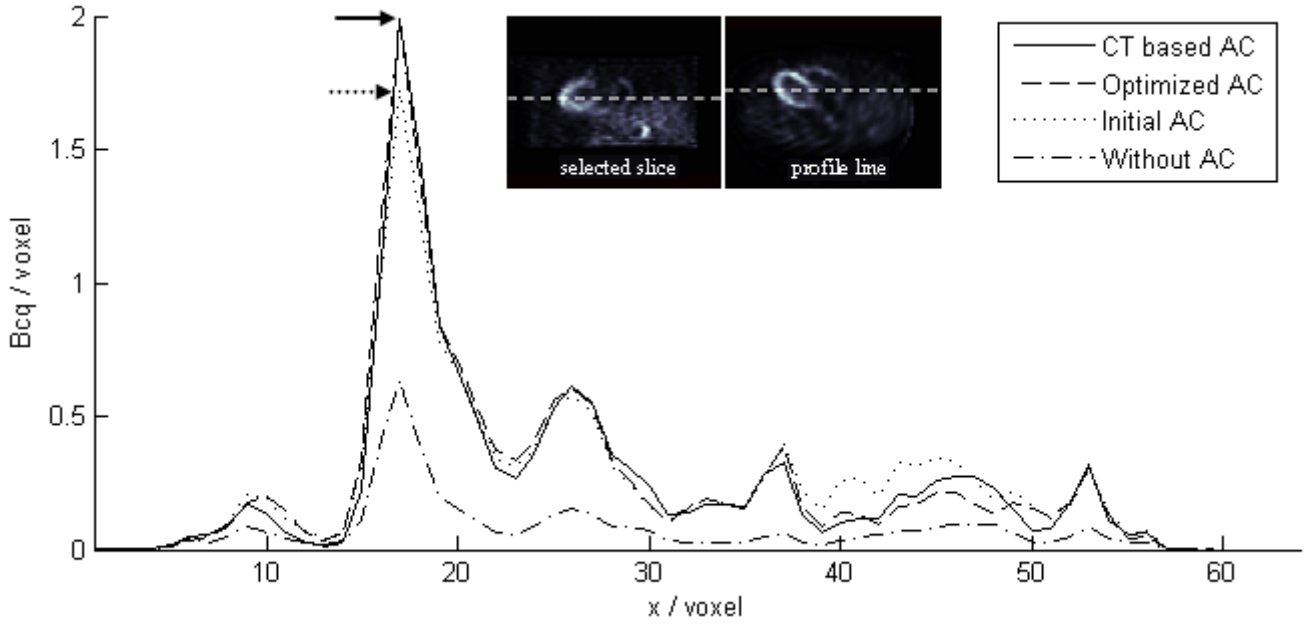

Figure 8: Comparison between reconstructed activity sections (180-degree-data) using several different attenuation maps for attenuation correction (AC)

5. CONCLUSIONS

The proposed method provides an alternative to perform attenuation corrected SPECT reconstructions solely from emission data. Applied to simulated phantom and real measured patient data, the algorithm was able to automatically detect and diminish inconsistencies between measured and estimated SPECT sinogram data. Thus, especially the final estimate for the activity distribution but also for the attenuation map has shown to be in good agreement with the reference data. It can be concluded that an initial attenuation map representing the typical anatomy of a target region can be effectively improved by the proposed iterative simultaneous reconstruction scheme. Compared to other simultaneous reconstruction approaches, the proposed use of a-priori information such as typical attenuation coefficients and anatomic information has shown to reduce cross-talk effects between the estimated activity and attenuation distribution. Moreover, since the algorithm automatically adapts to patient specific anatomy, it provides a special robustness, which makes it applicable for a large variety of patient types (e.g. regarding size, weight, organ extents, anatomical anomalies, etc.). However, although an improvement of the activity estimation was observed in all our tests, missing or inconsistent information about the attenuation has shown to impact the quality of the estimated attenuation map. Truncation of projections or a limited scan angle can result in a local mismatch of the computed attenuation map compared to reference data generated e.g. using transmission sources. As more and more adipose patients are scanned and big bore scanners are not yet widely available, it is suggested that these effects and their compensation are further investigated. Nevertheless, if there is no diagnostic need to perform an extra CT scan the proposed method offers an attractive opportunity to perform attenuation corrected SPECT reconstruction without additional transmission scans.

REFERENCES

[1] Botterweck, H., Bippus R., Goedicke A., Salomon A., Wieczorek H., "Quantitative Simultaneous Multiple Isotope SPECT Imaging with Iterative Monte-Carlo Reconstruction", Fully 3D (2007)

[2] King, M. A., Farncombe, P., "An overview of attenuation and scatter correction of planar and SPECT data for dosimetry studies", Cancer Biotherapy & Radiopharmaceuticals, 18(2), 181-190 (2003)

[3] King, M. A., Tsui, B. M., Pan, T. S., "Attenuation compensation for cardiac single-photon emission computed tomographic imaging: Part 1. Impact of attenuation and methods of estimating attenuation maps", J Nucl Cardiol, 2, 513-52 (1995)

[4] Celler, A., Dixon, K. L., Chang, Z., Blinder, S., Powe, J., Harrop, R., "Problems Created in Attenuation-Corrected SPECT Images by Artifacts in Attenuation Maps: A Simulation Study", J Nucl Med, 46, 335-343 (2005)

[5] Merhige, M. E. et al., "Impact of myocardial perfusion imaging with PET and (82)Rb on downstream invasive procedure utilization, costs, and outcomes in coronary disease management.", J Nucl Med, 48, 1069-1076 (2007)

[6] Natterer F., "Computerized tomography with unknown sources", SIAM, J. Appl. Math, 43, 1201-1202 (1983)

[7] Bronnikov, A., "Approximate reconstruction of attenuation map in SPECT imaging", IEEE Trans. Nucl. Sci., 42, 1483-1488 (1995)

[8] Sidky, E., Pan, X., "Mathematical formulation of the potato peeler perspective", IEEE Nucl. Sci. Symp. Conf. Record, 2, 722-725 (2002)

[9] Natterer, F., "Determination of tissue attenuation in emission tomography of optically dense media", Inverse Problems, 9 (6), 731–736 (1993)

[10] Laurette, I., Clackdoyle, R., Welch, A., Natterer F., Gullberg, G. T., "Comparison of Three Applications of ConTraSPECT", IEEE Trans. Nucl. Sci., 46, 2146-2153 (1999)

[11] Kudo, H., Nakamura, H., "A new approach to SPECT attenuation correction without transmission measurements", IEEE Nuc. Sci. Symp. Conf. Record, 2, 13/58-13/62 (2000)

[12] Dicken, V., "A new approach towards simultaneous activity and attenuation reconstruction in emission tomography", Inverse Problems, 15, 931-960 (1999)

[13] Nuyts, J. et al., "Simultaneous maximum a posteriori reconstruction of attenuation and activity distributions from emission sinograms", IEEE Trans. Med. Imaging, 18, 393-403 (1999)

[14] Krol, A., Bowsher, J., Manglos, S., Feiglin, D., Tornai, M., Thomas, F., "An EM algorithm for estimating SPECT emission and transmission parameters from emission data only", IEEE Trans. Med. Imaging, 20, 218-232 (2001)

[15] Case, J., King, M. A., Luo, D., Soares, E., Rabin, M., "Determination of concave body outlines from SPECT projection data", IEEE Nucl. Sci. Symp. and Med. Imaging Conf. Record, 2, 944-948 (1995)

[16] Shepp, L. A., Vardi, Y., "Maximum likelihood reconstruction for emission tomography.", IEEE Trans. Med. Imaging, 1, 113-122 (1982)

[17] Hudson, H. M., Larkin, R. S., "Accelerated image reconstruction using ordered subsets of projection data.", IEEE Trans. Med. Imaging, 13, 601-609 (1994)

[18] Segars, W. P., "Development and application of the new dynamic NURBS-based cardiac-torso (NCAT) phantom", Biomedical Engineering, University of North Carolina: Chapel Hill, NC (2001)

[19] Goedicke, A., Schweizer, B., Staelens, S., De Beenhouwer, J., "Fast simulation of realistic SPECT projections using forced detection in Geant4", Proceedings of the 3rd European Medical and Biological Engineering Conference, Praag, p. 6 (2005)